encit 2020

ABCM
Associação Brasileira de Engenharia e Ciências Mecânicas

18th Brazilian Congress of Thermal Sciences and Engineering
November 16-20, 2020 (Online)

ENC-2020-0073
Compressibility effects on the onset of dynamic stall in a periodic plunging airfoil

Renato Fuzaro Miotto
William Roberto Wolf
School of Mechanical Engineering, State University of Campinas, Campinas, SP, 13083-860, Brazil
miotto@fem.unicamp.br

Abstract. *The effects of compressibility on the onset of the dynamic stall vortex (DSV) over a wing section are analyzed by means of large eddy simulations. A SD7003 airfoil is considered at two different freestream Mach numbers, being* $M_\infty = 0.1$ *and* 0.4*, and at a chord-based Reynolds numbers of* $Re_c = 6 \times 10^4$*. The profile undergoes a periodic plunging motion. Results show that compressibility causes the DSV to form further downstream the leading edge. Moreover, higher compressibility also leads to weaker DSVs with lower residency time. For the current flow configuration and airfoil kinematics, the mechanisms of dynamic stall onset involve the upstream propagation of Kelvin-Helmholtz instabilities that trigger separation of a shear layer formed at the leading edge. In order to better characterize the onset of the DSV, two empirical criteria are assessed for the cases investigated: the leading edge suction parameter and the chord normal shear layer height. The application of both criteria show that the leading edge suction parameter is highly dependent on compressibility.*

Keywords: *dynamic stall, large eddy simulations, unsteady aerodynamics, onset of dynamic stall vortex*

1. Introduction

Dynamic stall is a flow condition frequently associated with an increase in unsteady loading that leads to large torsional forces and mechanical vibrations on a wing or blade. This condition has significant influence on the performance and fatigue life of several mechanical systems, such as helicopter rotors, wind turbines and flapping wing aerial vehicles. Hence, understanding the dynamic stall phenomenon is of paramount importance to predict performance parameters and improving the design of the previously-mentioned engineering devices.

Attempts to reproduce and describe dynamic stall by computational means were carried out by several groups and a review is provided by Ekaterinaris and Platzer (1998). Reynolds-averaged Navier-Stokes (RANS) computations, and their unsteady counterpart (URANS), have been employed for probing massively separated flows. These techniques should be used with a judicious choice of proper turbulence models. Although continually employed (Costes *et al.* (2015); Kaufmann *et al.* (2017)), these formulations cannot be expected to truly predict the dynamic stall phenomenon given the complex flow physics at play near the leading edge. In particular, viscous mechanisms such as boundary layer development, incipient separation and noise generation (Nagarajan *et al.* (2006)) that occur in dynamic stall are hardly characterized from a RANS perspective, although advances are being made in this area (see Bernardos *et al.* (2019) for instance). Similar limitations also apply to experimental studies that rely on flow visualizations or low spatio-temporal resolution techniques. The lack of information about the events occurring inside the boundary layer end up limiting the exploration of active flow sensing, control strategies and the development of new turbulence and reduced-order models for dynamic stall.

Currently, with recent progress in numerical methods and the tremendous increase in computational power, high-fidelity numerical simulations can be used as a predictive tool in the design stage. In this sense, wall-resolved large eddy simulations (LES) are increasingly being used to address the onset of dynamic stall at a broad range of Reynolds numbers, providing essential information about the boundary layer dynamics, including its separation. Motivated by micro air vehicle applications, the first investigations of dynamic stall under a transitional flow regime using implicit large eddy simulations (ILES) were presented by Visbal (2009); Garmann and Visbal (2011), and Visbal (2011). They observed that, at low Reynolds numbers ($\mathrm{Re}_c \approx 10^4$), transition effects played a critical role in the leading edge vortex dynamics and aerodynamic coefficients, even when the incipient separation and dynamic stall vortex formation were initially laminar. The leading edge vortices were found to experience an abrupt breakdown into fine-scale turbulence due to spanwise instabilities. This resulted in a subsequent vorticity cancellation that, in turn, led to a rapid reduction of the

maximum values of phase-averaged vorticity. These investigations were further extended to higher Reynolds numbers ($\mathrm{Re}_c = 0.2 \times 10^6$ and 0.5×10^6) for a constant pitching rate motion by Visbal (2014), where it was found that the onset of dynamic stall is characterized by the presence of a laminar separation bubble (LSB) near the leading edge.

Having an indication of massive dynamic flow separation near the leading edge is of paramount importance for understanding the onset of dynamic stall. This would allow the construction of dynamic stall models and the definition of control strategies for mitigation of the DSV. In that sense, Ramesh *et al.* (2014) proposed a new stall onset criterion based on the idea that an airfoil can support a maximum amount of leading edge suction. By calculating the first term of the Fourier series for the distribution of a vortex sheet along the camber line using thin airfoil theory, they have numerically observed a critical threshold of suction when the leading edge vortex is being formed. When this limit is exceeded, vorticity is released from the leading edge giving rise to the dynamic stall vortex. The term was referred to as leading edge suction parameter (LESP) and it depends on the airfoil shape and flow Reynolds number.

According to the previous authors, it should be independent of the airfoil kinematics, except in scenarios where a large trailing edge flow separation is present. Since most occurrences of dynamic stall exhibit some degree of trailing edge separation and flow reversal, a new quantifiable feature was proposed by Deparday and Mulleners (2019) to predict the dynamic stall vortex inception. In their new approach, critical values of the chord normal shear layer height and the airfoil circulation were observed to be invariant to motion and, thereby, being better indicators of the dynamic stall onset. These authors also improved the LESP model to account for the shear layer evolution effects during the stall development. However, nothing was said about how compressibility affects the applicability and reliability of these criteria. Moreover, the shear layer height criterion was never applied for airfoils under ramp conditions, where the effective angle of attack increases with a constant rate.

Wall-resolved LES provides great detail of the unsteady boundary layer characteristics in dynamic stall. This is an important aspect that may help with exploration of flow control strategies for unsteady airfoils. Motivated by this fact, in the present work, we apply ILES to investigate the flow features responsible for the inception of the dynamic stall vortex. An assessment of the different approaches used by Deparday and Mulleners (2019) to characterize onset of the dynamic stall vortex is also presented considering the effects of compressibility.

2. METHODOLOGY

The numerical scheme employed for the spatial discretization is a sixth-order accurate compact scheme implemented on a staggered grid. High-wavenumber compact filtering is applied to the computed solution at prescribed time intervals to control numerical instabilities. For time integration, an explicit third-order compact storage Runge-Kutta scheme (Wray (1986)) is applied far from solid boundaries and an implicit modified second-order Beam-Warming scheme (Beam and Warming (1978)) is used in the near-wall region to overcome the time step restriction typical of wall-resolved LES. Sponge layers and characteristic boundary conditions based on Riemann invariants are applied at inflow and outflow boundaries and adiabatic no-slip boundary conditions are applied at solid boundaries. Details regarding the numerical formulation are given in Nagarajan *et al.* (2003). It is worth mentioning that the code used in the present study has been previously validated for dynamic stall configurations (see Ramos *et al.* (2019)).

3. RESULTS

Two different freestream Mach numbers are investigated in this work to assess compressibility effects on dynamic stall of plunging airfoils. Here, the values $M_\infty = 0.1$ and 0.4 are used, being the former also studied in Visbal (2011); Ramos *et al.* (2019) and Mohan *et al.* (2016). The mesh refinement and domain extension studies were discussed by the references cited previously and, in the present work, we employ the same grid resolution used by Ramos *et al.* (2019), which has $480 \times 350 \times 96$ (≈ 16 million) points along a $s/c = 0.4$ span. The studied configuration comprises an SD7003 airfoil at $\alpha_0 = 8$ deg. static angle of attack. The airfoil trailing edge is rounded with an arc of radius $r/c = 0.0008$ to facilitate the use of an O-mesh topology and to keep metric terms smooth.

When the airfoil is subjected to periodic motion, the airfoil vertical displacement $h(t)$ is specified as

$$h(t) = h_0 \sin(2kt). \tag{1}$$

The motion amplitude h is a function of nondimensional time t, reduced-frequency k and maximum plunge amplitude h_0. Here, the parameters are set as $k = 0.25$ and $h_0 = 0.5$ to reproduce the flow configuration studied by Visbal (2011); Ramos *et al.* (2019). Although the numerical formulation uses a non-dimensionalization of flow velocities and time scale by speed of sound, the parameters in Eq. 1 are based on the freestream velocity, similarly to the previous references. The maximum plunging amplitude is normalized by the chord length. For the present plunging motion, the airfoil undergoes a variation in effective angle of attack in the range of $-6^\circ \leq \alpha_{eff} \leq 22^\circ$.

The first cycle is discarded from the analysis since it contains transient features from the numerical procedure, which assumes an initial uniform flow in the entire domain. Results for the periodic plunging cases are shown only for the second cycle and, although cycle-to-cycle variations indeed occur, we emphasize that the effort of the present work is to focus on

the onset of dynamic stall, where one cycle should be sufficient to capture the main trends associated with the formation of the dynamic stall vortex (DSV). Phase-averaged results of this case can be found in Visbal (2011) and Ramos *et al.* (2019), and the effects of cycle-to-cycle variations is discussed in Ramos *et al.* (2019). It is also important to note that, differently from the cited references, here, we define the reference position for the phase angle $\phi = 0$ at $h(t) = 0$ and not at the topmost position $h(t) = h_0 = 0.5$. Therefore, at $\phi = 0$ the airfoil is moving upward with maximum vertical velocity. The airfoil reaches the topmost position at $\phi = 90$ with zero vertical velocity and, then, starts the descending motion. At $\phi = 180$ it has the maximum downward velocity and at $\phi = 270$ it reaches the bottom-most position. Then, it moves upward and repeats the cycle.

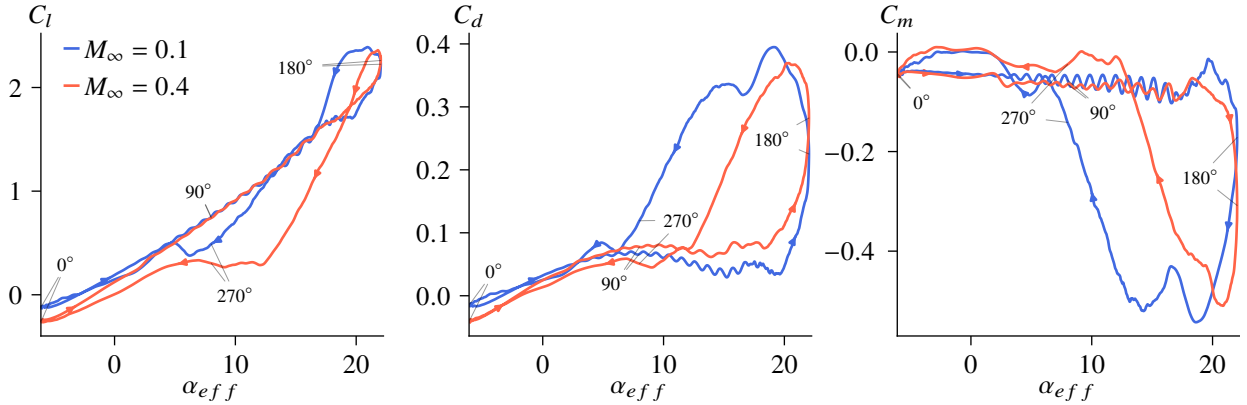

Figure 1. Lift, drag and pitching moment coefficients as a function of the effective angle of attack for $M_\infty = 0.1$ and $M_\infty = 0.4$ (periodic motion).

Figure 1 shows the lift (C_l), drag (C_d) and pitching moment (C_m) coefficients as a function of the effective angle of attack for freestream Mach numbers $M_\infty = 0.1$ and $M_\infty = 0.4$. The phase angle ϕ is also shown in the plots for particular instants of the motion. It is observed that compressibility effects act on the sense to attenuate the aerodynamic loads in the hysteresis loop, while maintaining the maximum and minimum values, a trend that was also observed by Sangwan *et al.* (2017) for a two-dimensional simulation of a pitching airfoil at high Reynolds number. Here, we observe that the highest discrepancies in C_l and C_d between the two compressible regimes occur when the effective angle of attack is reduced from $\alpha_{eff} \approx 18°$ to $10°$, which corresponds to the time interval when the airfoil is ceasing its downstroke motion. At $\alpha_{eff} = 8°$, the airfoil is at the bottom-most position for the downstroke. These results, specially the accentuated decay of the coefficients during the post-stall period with the increasing Mach number, can be better understood from Figs. 2 and 3. The former exhibits the spanwise-averaged pressure coefficient (C_p) contours at different flow instants for the two Mach numbers investigated. The formation of the DSV is also shown in gray shade using a flow entropy measure. The latter figure presents the full history of skin friction coefficient (C_f) along the suction side of the airfoil.

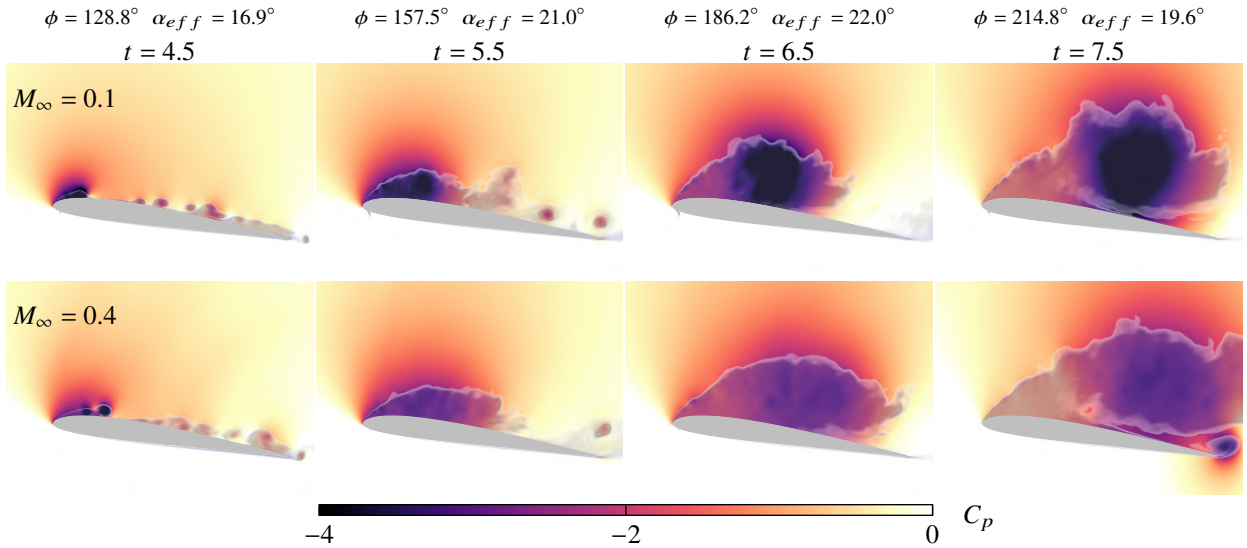

Figure 2. Spanwise-averaged pressure coefficients at different time flow instants for $M_\infty = 0.1$ (top) and $M_\infty = 0.4$ (bottom) computed for the periodic motion.

From Fig. 2, two immediate observations can be drawn. The first is that the pressure core of the DSV is weakened for

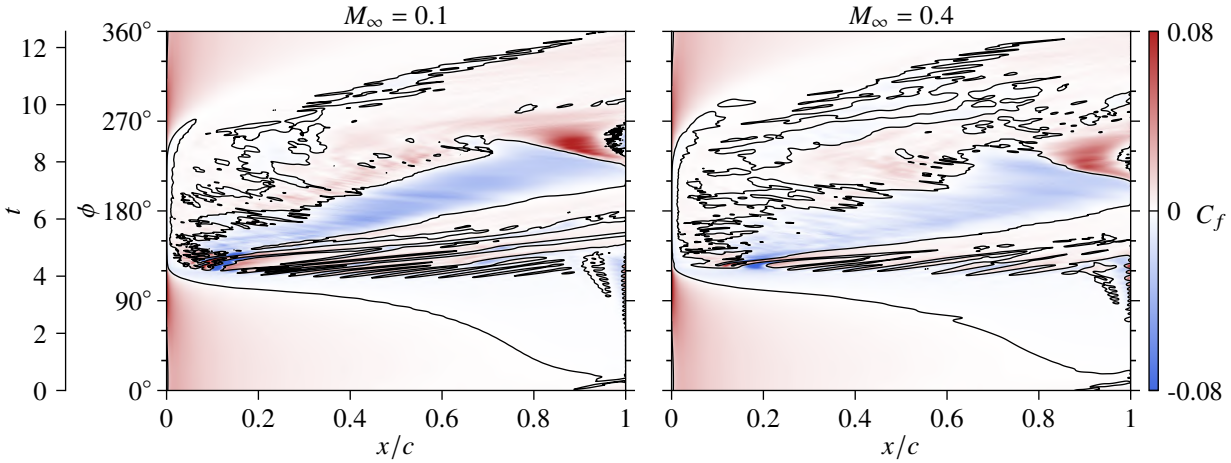

Figure 3. Comparison of skin friction coefficient for $M_\infty = 0.1$ (left) and $M_\infty = 0.4$ (right) computed for the periodic motion. Black contours stand for $C_f = 0$ values, dividing positive and negative contours.

the higher Mach number flow. The second concerns the gestation period and residence time for which the DSV remains over the airfoil. It is observed that such time is reduced with an increase in Mach number. A heuristic reasoning to explain the weakening of the DSV strength with compressibility is provided by Chandrasekhara and Carr (1990). They argue that, for higher Mach numbers, the pressure gradient is reduced near the leading edge due to the smaller curvature of the streamlines from the earlier flow separation. At this condition, the net vorticity introduced is smaller, which leads to a weaker vortex formation. As observed from Fig. 2, the DSV residence time is also smaller for the the $M_\infty = 0.4$ flow. The figure shows that, at $t = 6.5$, the DSV is more spread for the higher Mach number flow, spanning the entire airfoil chord. On the other hand, it is lumped at the mid-chord location for the lower Mach number case. At $t = 7.5$, the DSV is already leaving the airfoil surface for the higher Mach number flow, being pushed by a trailing edge vortex.

The C_f plots in Fig. 3 present further information about the flow history over the suction side of the airfoil. The presence of high-frequency C_f variations along the chord can be observed in the range $120 < \phi < 130°$ for both flow conditions but they are more pronounced for the $M_\infty = 0.1$ case. These fluctuations are due to Kelvin-Helmholtz instabilities forming during the downstroke motion. Figure 4 shows this primary instability stage of the flow at different instants using contours of entropy. As one can see, the instabilities arise initially at the trailing edge but rapidly develop along the entire suction side. They form at an earlier time for the lower Mach number and exhibit a more packed behavior where flow structures have a higher wavenumber.

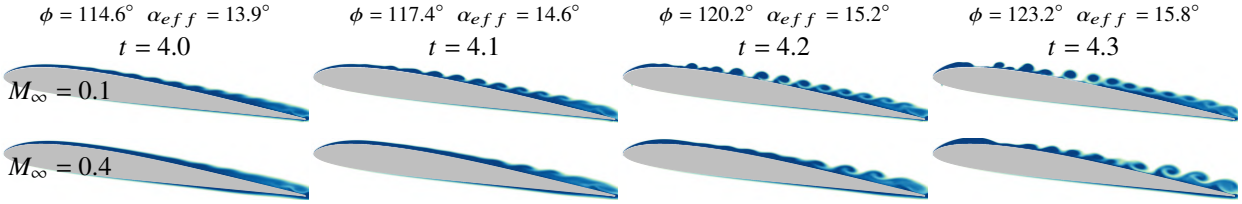

Figure 4. Contours of entropy showing the primary instability stage for $M_\infty = 0.1$ (top) and $M_\infty = 0.4$ (bottom) for the periodic motion.

For both cases investigated, the formation of the dynamic stall vortex appears just after the primary instability stage, at a phase angle $\phi \approx 135$. The traveling signature of the DSV can be noticed by the negative C_f values shown in blue contours along the airfoil chord for intermediate phase angles ϕ. A visual comparison of the plots confirms the faster transport of the DSV for $M_\infty = 0.4$. One can also observe that the formation of the trailing edge vortex takes place earlier and with less intensity for this case. The weaker signature of friction coefficient for $M_\infty = 0.4$ is also noticed compared to that for $M_\infty = 0.1$. This can be observed by the darker blue contours depicted for C_f in the lower Mach number flow. In this context, velocity variations normal to the surface are smoother for the higher Mach number, a point that will be addressed later.

By observing the skin friction maps in Fig. 3 we notice the presence of a flow reversal in light blue color that progressively advances over the airfoil suction side from the trailing edge region as ϕ increases. The time (here also visualized as a function of the plunge cycle angle ϕ) in which the flow reversal along the chord initiates does not appear to change under the distinct compressible regimes investigated. The main differences in C_f between the two flows start after the beginning of the primary instabilities, which are more sparse for the higher Mach number flow. As mentioned before, the transport of the DSV over the suction side is faster for $M_\infty = 0.4$ and the vortical structure is more diffused. Moreover,

the point where the development of the dynamic stall vortex occurs moves from approximately $x/c = 0.1$ for $M_\infty = 0.1$ to $x/c = 0.2$ for $M_\infty = 0.4$. This behavior can be better understood through an inspection of the boundary layer forming over the airfoil suction side. Figure 5 shows the spanwise-averaged z-vorticity contours at a short time window ($\Delta t = 0.3$, based on the freestream velocity, which corresponds to nearly 2.4% of the plunging cycle period) that marks the moment of the formation of the DSV.

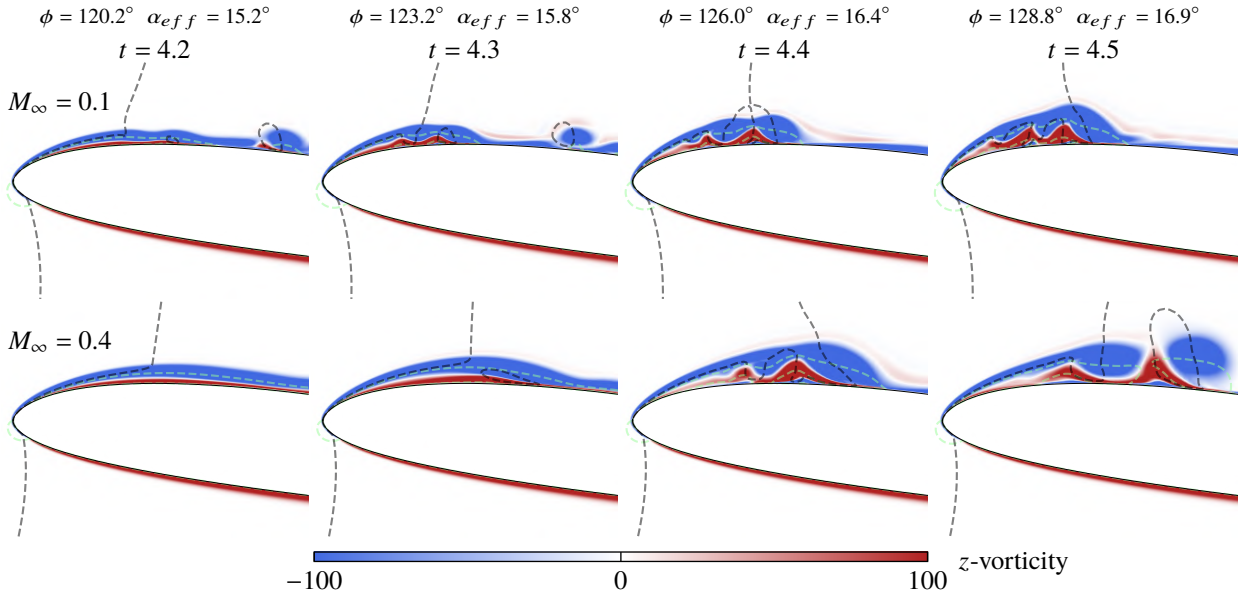

Figure 5. Spanwise-averaged z-vorticity field near the leading edge ($x/c \leq 0.25$) revealing the sudden boundary layer separation for $M_\infty = 0.1$ (top) and $M_\infty = 0.4$ (bottom) for the periodic motion. Dashed lines represent positions where $u = 0$ (green) and $v = 0$ (black) and indicate flow regions where velocity components change direction.

Differently from steady separation, in dynamic stall the outer flow continues to follow the airfoil contour besides the presence of flow reversal. As a consequence, a local shear layer forms between the displaced leading edge boundary layer and the reversed fluid layer which is, at a later stage, subjected to inflectional instabilities. This leads to the generation and growth of coherent structures that can be visualized in Fig. 5. In the same figure, auxiliary lines are also plotted to indicate regions where u- and v-velocity components change directions, from which we see the presence of flow reversal and the shear layer over the leading edge.

In previous work by van Dommelen and Shen (1980), it is speculated that the onset of the unsteady separation phenomenon is an inviscid process, independent of the Reynolds number. This characteristic is attributed to the fact that the initial flow reversal along the surface, which is triggered by a strong adverse pressure gradient, is later governed by inertial effects along the zero vorticity line. Along this line, formed as the fluid particles approach the separation region, the convective terms dominate over the viscous and pressure effects justifying the inviscid assumption. Under the influence of the increasing adverse pressure gradient, the local reversed flow begins to accelerate rapidly inside the leading edge region causing collisions between particles traveling at different speeds. Because of the presence of the solid surface, particles are propelled away from the wall. Meanwhile, the vorticity conservation yields an outward distortion of the zero vorticity line, destabilizing the local vorticity distribution and resulting in the formation of a large vortical structure. The development of this vortex and its induced secondary separation lead to its ejection from the surface.

The process described above can be visualized in Fig. 6, where the local Mach number is plotted along with the zero-vorticity lines during the dynamic stall onset. In this figure, the laminar flow continues to accelerate up to a point further downstream the leading edge where it encounters the flow reversal accelerating along an inner layer. In this region, mutual interaction seems to occur between the outer flow and the flow inside the zero vorticity line. Both flows accelerate in opposite directions forming a low pressure core and spots of supercritical flow. The flow, however, is decelerated isentropically and no shock waves are observed despite the sonic flow regions present in the $M_\infty = 0.4$ case. In this case, a strong acceleration of the flow reversal, sufficient to achieve sonic speeds, occurs along the zero vorticity lines. The particle collision accompanied by the low pressure on the aft portion of the separation region results in the flow reversal being ejected away from the surface and interacting with the outer flow, what creates a large vortical structure that intensifies the instabilities in the region. The dynamics observed in Figs. 5 and 6 appear to agree well with the overall concept of the van Dommelen and Shen model, which provides the description of the flow up to the early stages of separation.

As observed from the figures, the onset of the DSV takes place further downstream from the leading edge with an increase in Mach number. Chandrasekhara and Carr (1990) suggest that leading edge separation occurs at an earlier time

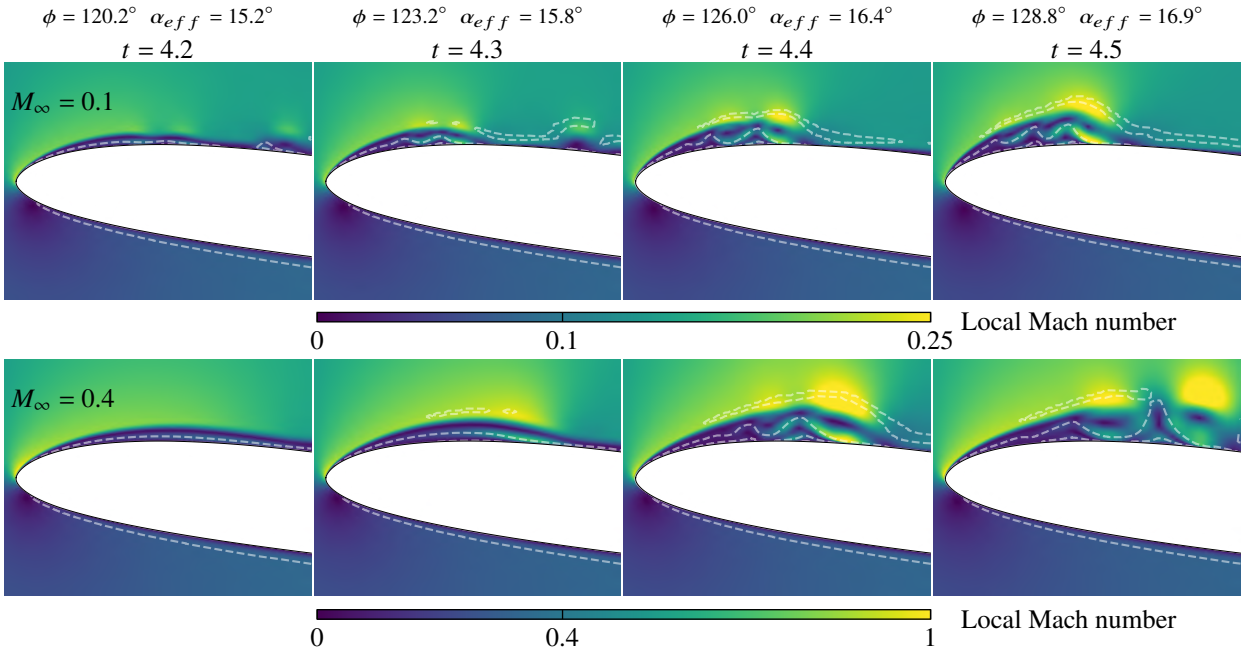

Figure 6. Local Mach number contours near the leading edge ($x/c \leq 0.25$) for $M_\infty = 0.1$ (top) and $M_\infty = 0.4$ (bottom) for the periodic motion. Dashed contours represent the zero-vorticity lines.

due to compressibility effects. Therefore, a higher Mach number would cause separation at a lower effective angle of attack. This earlier separation for higher Mach numbers would then occur for a flow where the curvatures of streamlines are less pronounced and the pressure gradient is weaker. However, this earlier separation is not observed in the present simulations, suggesting that the pressure gradient reduction may not be a direct consequence of the lower effective angle of attack. For the present periodic motion, the leading edge separation seems to be related to the primary instabilities developed at the trailing edge region and later along the entire airfoil suction side as shown in Fig. 4. As can be seen in Fig. 7, these instabilities reach the leading edge region and interact with the secondary instability presented in Figs. 5 and 6. As can be observed from Fig. 4, the primary instabilities reach further upstream for the $M_\infty = 0.1$ case. On the other hand, for $M_\infty = 0.4$, one can observe a wider region of favorable pressure gradient along the leading edge and that delays the formation of secondary instabilities. As discussed by Li *et al.* (2019), compressibility has a stabilizing effect that delays the laminar to turbulence transition in free shear flows. Here, the mechanism appears to be similar although the plunging motion together with the surface presence lead to a more complex flow.

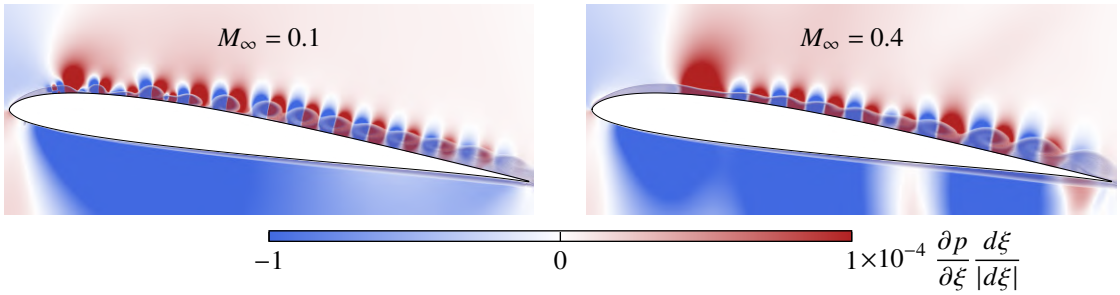

Figure 7. Pressure gradient contours in ξ direction and contours of entropy for $M_\infty = 0.1$ (top) and $M_\infty = 0.4$ (bottom) for periodic motion at $t = 4.25$.

Analysis of leading edge suction parameter and shear layer height

As discussed by Ramesh *et al.* (2014), the LESP parameter A_0 can be used to indicate the onset of the dynamic stall vortex, which occurs when the maximum value of this parameter is achieved. According to Deparday and Mulleners (2019), the LESP can be computed directly from numerical or experimental data as

$$A_0 = \text{sgn}[\cos(\lambda - \alpha)]\sqrt{\frac{2}{\pi}\|\vec{S}_{LE}\|\,|\cos(\lambda - \alpha)|}. \tag{2}$$

In Eq. 2, α is the effective angle of attack and λ is the angle formed between the incoming flow and the leading edge suction vector $\vec{S}_{LE}$. This vector is determined by integrating the pressure signals from the first 10% extension of the airfoil chord. Hence, $\vec{S}_{LE}$ gives the net force from the surface pressure integration. Here, the sign function is included to yield a continuous result when $\cos(\lambda - \alpha)$ goes from positive to negative and vice-versa. A schematic representation of the terms used to evaluate A_0 according to Deparday and Mulleners (2019) is presented in Fig. 8 (a). In this figure, the 10% frontal portion of the airfoil chord is colored in blue and the chord line is shown as a dashed line.

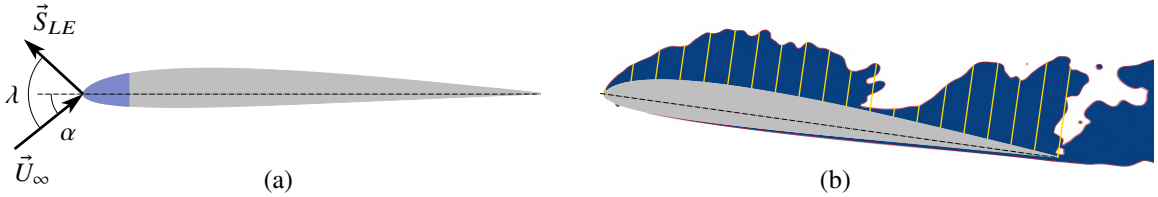

Figure 8. Schematic of the relevant parameters used in the calculation of the LESP (a) and entropy measure showing the evaluation of the chord normal shear layer height (b).

The temporal evolution of the leading edge suction parameter for the periodic airfoil motion is shown in the left hand side of Fig. 9 for the two Mach numbers investigated. Relevant values of the phase angle ϕ are marked in the figure and the green and purple dots are the LESP thresholds, plotted along with their respective coordinates (A_0, t). The green dots represent the first local maxima found in A_0 while the purple dots show the global maximum. According to the previous references, the global maximum should indicate the instant of DSV onset. However, we find here that the first local maximum provides a better estimate for the onset. Deparday and Mulleners (2019) show that after the onset of the DSV, the LESP is susceptible to noise from turbulence. It could be that the noise is impacting the calculation of the LESP in this case leading to new maximum values. Hence, the green dots will be used to provide the time instant of DSV onset.

Comparing the blue and red lines from Fig. 9, which correspond to the A_0 for Mach numbers $M_\infty = 0.1$ and $M_\infty = 0.4$, respectively, we notice that the maximum suction is reduced as compressibility increases. This is a consequence of the weaker low pressure core formed close to the leading edge during the onset of dynamic stall (see Fig. 2) and that directly influences the magnitude of the suction vector. The dynamic stall onset occurs almost at the same time for both cases.

The applicability and reliability of the LESP hinge upon a prior knowledge of the critical thresholds of the leading edge suction as a function of the parameters of the airfoil motion. However, the dependency of this suction to the kinematics and flow compressibility impairs its usage as a universal dynamic stall onset indicator for several realistic flow applications. With the aim to overcome this limitation, the shear layer height criterion proposed by Deparday and Mulleners (2019) was shown to be a more precise, motion independent, indicator although not easily accessible outside of a laboratory environment. In their work, the shear layer height was evaluated through an averaged location of clockwise rotating shear layer vortices identified using an Eulerian vortex criterion from the individual snapshots of the velocity field. Here, as we know the values of all conserved variables from the numerical simulation, it is possible to estimate the chord normal shear layer height, Δz, in a simpler manner. We compute contours of an entropy measure and select a small threshold (0.005 in this case) as a limit for the viscous region. A representation of the procedure is shown in Fig. 8 (b), where the blue region indicates the portion of the fluid within the limit where entropy values change above the 0.005 threshold. Then, uniformly distributed chord normal lines are drawn and their distances from the airfoil surface to the entropy contour boundary are measured. These lines are represented in Fig. 8 (b) in yellow color. When a given chord normal line intersects the limiting entropy level more than once, for instance, in the rightmost yellow line in the figure, a distance is computed for each intersection. Finally, all distances are averaged out to obtain Δz.

The temporal evolution of Δz for the two Mach number flows is shown in the right hand side of Fig. 9. From this figure, we see that during the lifetime of the dynamic stall vortex the shear layer height exhibits a high-frequency oscillatory behavior. This is a consequence of locally non-convex topological spaces formed when the flow is highly separated, causing the normal lines to have multiple intersections. This noise, however, do not harm the capability of the method to find the critical shear layer height since it is obtained by the intersection of two linear fits. According to Deparday and Mulleners (2019), these fits are comprised by the primary instability stage given by the horizontal line in Fig. 9, and the vortex formation stage represented by the first slope crossing the horizontal line. For our simulations, the instant of formation of the DSV is marked by the intersection of the green dashed lines shown in Fig. 9.

The threshold value of $\Delta z \approx 0.02$ based on the shear layer height remained the same for both Mach numbers. According to Deparday and Mulleners (2019), this critical value of Δz is invariant with respect to the kinematics. For the present periodical motion, we find that it is also invariant to the freestream Mach number. From Fig. 9, one can see that the time instant shown in the abscissa of the first local maximum value of the LESP shows a reasonable match with that computed by the critical shear layer height. However, when the global maximum value of the LESP is used, it indicates a more advanced stage characterized by the roll up of the shear layer into a large scale dynamic stall vortex as the onset

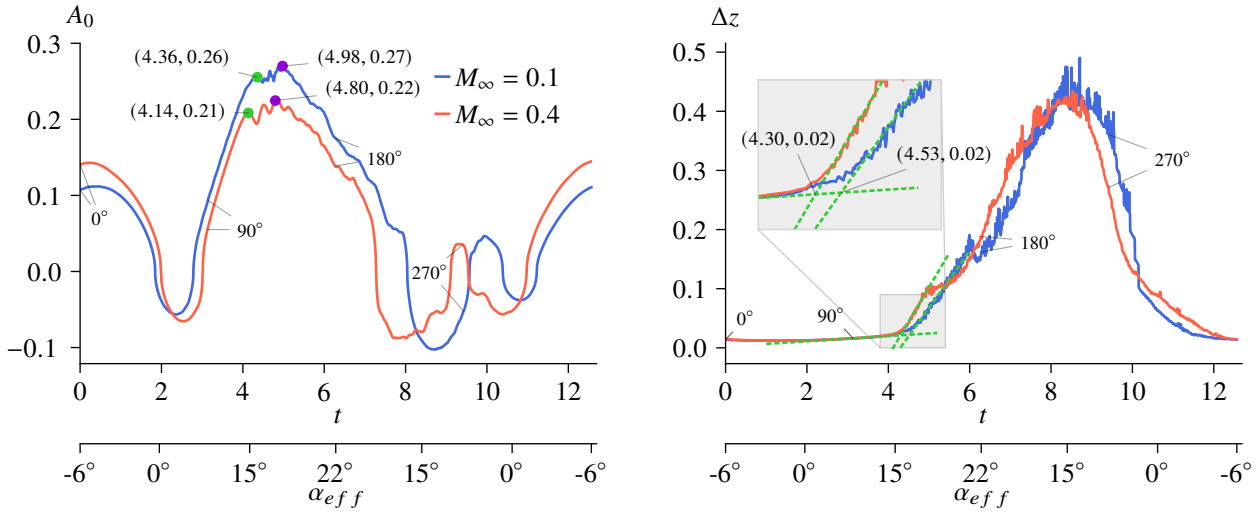

Figure 9. LESP and chord normal shear layer height for the airfoil in periodic motion at $M_\infty = 0.1$ and $M_\infty = 0.4$.

point. Despite the small time lapse between results from the two different methods, both answers are reasonable and consistent with the skin friction maps of Fig. 3.

4. Conclusions

Large eddy simulations are performed to investigate the effects of compressibility on the onset and evolution of dynamic stall for a SD7003 airfoil. In this study, the airfoil is subjected to a periodic plunging motion. The mechanisms of flow separation observed in the periodic plunging case seem to agree with the van Dommelen and Shen model for pitching airfoils. It is found that the onset period, residence time and strength of the dynamic stall vortex (DSV) decrease with an increasing Mach number, as previously reported for pitching airfoils. Descriptions of the primary instability stage, formed by Kelvin-Helmholtz instabilities due to flow reversal, and of the sudden breakdown of the vortical structures during the onset of dynamic stall are also provided.

In order to investigate the influence of compressibility on empirical indicators of dynamic stall onset, two recent criteria are employed, being the leading edge suction parameter (LESP) and the critical chord normal shear layer height, Δz. It is observed that the maximum suction is reduced as compressibility increases, revealing that the LESP is not only a function of the parameters of the airfoil motion but also of the freestream Mach number. The Δz criterion, on the other hand, appears to be almost invariant to the freestream Mach number.

5. ACKNOWLEDGEMENTS

The authors acknowledge FAPESP for the scholarships provided to the first author under grants No. 2017/10795-1 and No. 2019/02335-6. The Ohio Supercomputer Center (OSC), the CEPID-CeMEAI cluster Euler, and cluster SDumont (Project SIMTURB) are also acknowledged for providing the computational resources for this research. This work is also supported by FAPESP grants 2013/08293-7 and 2013/07375-0.

6. REFERENCES

Beam, R.M. and Warming, R.F., 1978. "An implicit factored scheme for the compressible Navier-Stokes equations". *AIAA Journal*, Vol. 16, No. 4, pp. 393–402.

Bernardos, L., Richez, F., Gleize, V. and Gerolymos, G.A., 2019. "Algebraic nonlocal transition modeling of laminar separation bubbles using k-w turbulence models". *AIAA Journal*, Vol. 57, No. 2, pp. 553–565. doi:10.2514/1.J057734.

Chandrasekhara, M.S. and Carr, L.W., 1990. "Flow visualization studies of the mach number effects on dynamic stall of an oscillating airfoil". *Journal of Aircraft*, Vol. 27, No. 6, pp. 516–522. doi:10.2514/3.25313.

Costes, M., Richez, F., Pape, A.L. and Gavériaux, R., 2015. "Numerical investigation of three-dimensional effects during dynamic stall". *Aerospace Science and Technology*, Vol. 47, pp. 216 – 237. ISSN 1270-9638. doi: https://doi.org/10.1016/j.ast.2015.09.025.

Deparday, J. and Mulleners, K., 2019. "Modeling the interplay between the shear layer and leading edge suction during dynamic stall". *Physics of Fluids*, Vol. 31, No. 10, p. 107104. doi:10.1063/1.5121312.

Ekaterinaris, J.A. and Platzer, M.F., 1998. "Computational prediction of airfoil dynamic stall". *Progress in Aerospace Sciences*, Vol. 33, No. 11, pp. 759 – 846. ISSN 0376-0421. doi:https://doi.org/10.1016/S0376-0421(97)00012-2.

Garmann, D.J. and Visbal, M.R., 2011. "Numerical investigation of transitional flow over a rapidly pitching plate". *Physics of Fluids*, Vol. 23, No. 9, p. 094106. doi:10.1063/1.3626407.

Kaufmann, K., Merz, C.B. and Gardner, A.D., 2017. "Dynamic stall simulations on a pitching finite wing". *Journal of Aircraft*, Vol. 54, No. 4, pp. 1303–1316. doi:10.2514/1.C034020.

Li, D., Komperda, J., Ghiasi, Z., Peyvan, A. and Mashayek, F., 2019. "Compressibility effects on the transition to turbulence in a spatially developing plane free shear layer". *Theoretical and Computational Fluid Dynamics*, Vol. 33, No. 6, pp. 577–602. ISSN 1432-2250. doi:10.1007/s00162-019-00507-w.

Mohan, A.T., Gaitonde, D.V. and Visbal, M.R., 2016. "Model reduction and analysis of deep dynamic stall on a plunging airfoil". *Computers and Fluids*, Vol. 129, pp. 1 – 19. ISSN 0045-7930. doi: https://doi.org/10.1016/j.compfluid.2016.01.017.

Nagarajan, S., Hahn, S. and Lele, S., 2006. "Prediction of sound generated by a pitching airfoil: A comparison of rans and les". In *12th AIAA/CEAS Aeroacoustics Conference*. doi:10.2514/6.2006-2516.

Nagarajan, S., Lele, S.K. and Ferziger, J.H., 2003. "A robust high-order compact method for large eddy simulation". *Journal of Computational Physics*, Vol. 191, No. 2, pp. 392–419.

Ramesh, K., Gopalarathnam, A., Granlund, K., Ol, M.V. and Edwards, J.R., 2014. "Discrete-vortex method with novel shedding criterion for unsteady aerofoil flows with intermittent leading-edge vortex shedding". *Journal of Fluid Mechanics*, Vol. 751, pp. 500–538.

Ramos, B.L.O., Wolf, W.R., Yeh, C.A. and Taira, K., 2019. "Active flow control for drag reduction of a plunging airfoil under deep dynamic stall". *Physical Review Fluids*, Vol. 4, p. 074603. doi:10.1103/PhysRevFluids.4.074603.

Sangwan, J., Sengupta, T.K. and Suchandra, P., 2017. "Investigation of compressibility effects on dynamic stall of pitching airfoil". *Physics of Fluids*, Vol. 29, No. 7, p. 076104. doi:10.1063/1.4995457.

van Dommelen, L. and Shen, S., 1980. "The spontaneous generation of the singularity in a separating laminar boundary layer". *Journal of Computational Physics*, Vol. 38, No. 2, pp. 125 – 140. ISSN 0021-9991. doi: https://doi.org/10.1016/0021-9991(80)90049-2.

Visbal, M.R., 2009. "High-fidelity simulation of transitional flows past a plunging airfoil". *AIAA Journal*, Vol. 47, No. 11, pp. 2685–2697. doi:10.2514/1.43038.

Visbal, M.R., 2011. "Numerical investigation of deep dynamic stall of a plunging airfoil". *AIAA Journal*, Vol. 49, No. 10, pp. 2152–2170. doi:10.2514/1.J050892.

Visbal, M.R., 2014. "Analysis of the onset of dynamic stall using high-fidelity large-eddy simulations". In *52nd Aerospace Sciences Meeting*.

Wray, A.A., 1986. "Very low storage time advancement schemes". In *NASA Technical Report 1999-209349*.

7. RESPONSIBILITY NOTICE

The authors are solely responsible for the printed material included in this paper.